ACS Sustainable Chemistry & Engineering

pubs.acs.org/journal/ascecg

Research Article

Carbon-Coated Catalytic Static Mixers for Dual-Function Liquid Organic Hydrogen Carrier Hydrogenation and Dehydrogenation

Marcel F G Disl, Derrick Ng, Jurie Swart, Franziska Auer, Stephan Kiermaier, Monica Distaso, Peter Wasserscheid, Christian H Hornung, and Zongli Xie*

Cite This: ACS Sustainable Chem. Eng. 2026, 14, 8210–8220

Read Online

ACCESS | Metrics & More | Article Recommendations | Supporting Information

ABSTRACT: The efficient immobilization of active catalyst materials onto surfaces of complex scaffold geometries remains a key challenge in the development of high-performance structured reactor systems. We demonstrate, for the first time, a carbon-based coating for the direct deposition of a carbon black-supported platinum catalyst onto an additively manufactured stainless steel catalytic static mixer (CSM). The conformal carbon-based coating provides mechanical stability comparable to that of conventional alumina supports while offering a chemically robust interface for catalyst immobilization. In liquid organic hydrogen carrier hydrogenation and dehydrogenation, the carbon-coated CSMs exhibit higher activity than industrial benchmark catalysts and reduced side product formation in the dehydrogenation, relative to alumina-based catalysts. Moreover, the carbon-based catalyst enables dual functionality within a single catalyst system, eliminating the need for separate hydrogenation and dehydrogenation catalysts. Beyond catalytic performance, the integration of the carbon coating with the structured stainless steel CSM architecture enhances heat/mass transfer and reduces pressure drop, offering distinct advantages over pelletized and slurry-based systems. The developed carbon-based CSM offers a versatile platform that extends the reach of carbon-based catalysis across diverse catalytic processes.

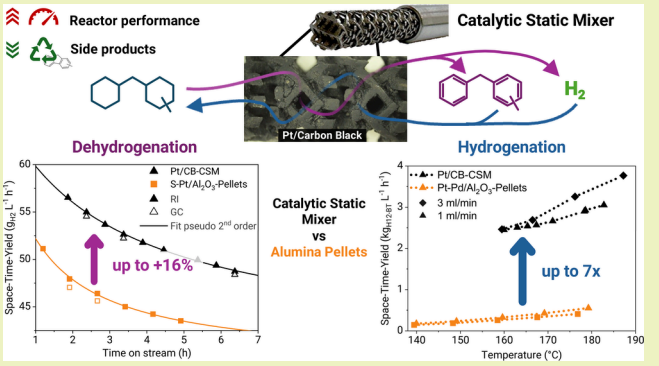

KEYWORDS: *carbon coating, catalytic static mixer, liquid organic hydrogen carrier, catalyst stability, structured catalysis, hydrogenation, dehydrogenation*

1. INTRODUCTION

Noble metal-based catalysis is widely used in industrial reactions and is gaining growing interest in emerging sustainable and renewable energy processes.[1−4] Achieving global sustainability goals requires continuous innovation of efficient and robust catalysts to address new challenges in chemical energy conversion.[1,4] Achieving these goals is contingent upon the optimization of metal efficiency and selectivity.[1,5,6] Carbon-based catalysts have attracted growing interest for environmental catalysis, energy conversion, and energy storage.[7,8] Carbon materials are valued for their high specific surface area, chemical inertness, and resistance to harsh reaction conditions.[7,8] Their tunable surface chemistry is a key feature, not only enabling metal-free carbon catalysis but also facilitating highly dispersed metal deposition and metal−support interactions.[1−4]

Typically, industrial heterogeneous catalysts like metal oxides are deployed in fixed-bed reactors as shaped bodies (pellets, extrudates, spheres, or granules) to achieve a practical balance of pressure drop, heat and mass transfer, and facilitate easy handling and loading of the catalyst.[5,6] Consequently, fine powders are rarely used directly in packed beds because they can cause excessive pressure drop and poor bed permeability.[6] Carbon supports span both regimes: activated carbon is commercially available and widely used in granular or extruded forms for fixed-bed operation (including precious-metal catalysts), whereas many high-surface-area nanocarbons (e.g., carbon black, graphene) are intrinsically fine powders and are therefore more commonly applied in slurry reactors or immobilized as wash coats/structured supports[6,7] Although carbon powders can be pelletized/extruded or processed into monoliths, achieving sufficient mechanical strength often requires binders and shaping steps that may partially block porosity or mask active sites, creating a trade-off between intrinsic catalyst utilization and reactor operability[6,8] In fixed-bed operation, pressure drop increases with throughput (and strongly with decreasing particle size), and intra/interparticle

Received: January 4, 2026
Revised: April 8, 2026
Accepted: April 9, 2026
Published: April 21, 2026

https://doi.org/10.1021/acssuschemeng.6c00102
ACS Sustainable Chem. Eng. 2026, 14, 8210−8220

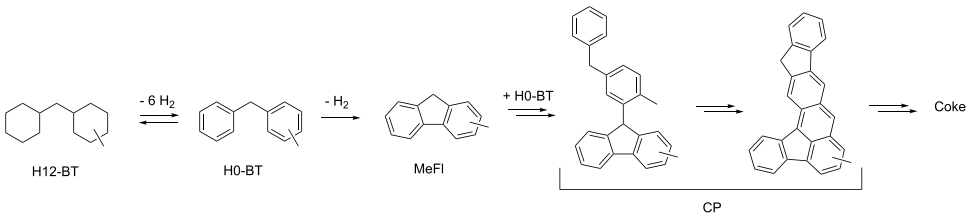

Figure 1. Perhydro benzyltoluene/benzyltoluene LOHC system with one example pathway for MeFl and CP formation. MeFl could also form from H6-BT. CP can also be formed from two MeFl molecules. Pathway from Henseler et al.[26]

heat and mass transfer can become rate-limiting, compromising temperature control and catalyst utilization at larger scales.[9,10] Slurry stirred-tank reactors can ease pressure drop constraints via intensive mixing, yet they may be limited by interphase transport (gas−liquid and liquid−solid) and introduce additional steps for catalyst recovery, which penalize process simplicity and scalability.[11]

Because pelletized fixed-bed reactors remain the industrial benchmark, systematic comparisons with structured reactor internals such as catalytic static mixers (CSMs) are essential to quantify how fluid dynamics and external transport phenomena influence the apparent catalyst performance.[12] CSMs provide a predictable, tunable flow field that minimizes flow maldistribution and improves heat management at low pressure drop; in direct packed bed vs CSM hydrogenation studies, conversion losses at high gas-to-liquid ratios were attributed to mass-transfer limitations in the packed bed, whereas the CSM maintained higher conversion/TOF consistent with mitigated transport limitations.[12]

These shortfalls present the primary constraint for industrial applications of carbon-based catalysts on scale.[11,13,14] While the utilization of slurry reactors can improve the heat management, compared to a packed bed, their application is predominantly restricted to laboratory settings and small-scale chemical processes such as the production of fine chemicals and pharmaceuticals, due to challenges in scale-up and the added complexity for product and catalyst separation.[11,13]

In several fields, the lack of suitable carbon-based supports has led to the use of carbon as a topcoat on catalysts to reduce their adverse characteristics.[15,16] A prominent example is the carbon coating of alumina-based catalysts in the Fischer−Tropsch synthesis, where the acid sites of alumina promote hydrocracking, isomerization, and aromatization side reactions.[16] Applying a thin carbon coating onto the prepared metal particle alumina-based catalyst shields the acidic sites of alumina, while preserving the active metal surface. This carbon coating approach leads to increased selectivity by suppressing side reactions induced by acidic sites of alumina support, which are rendered inaccessible by the carbon layer and additionally enhances nanoparticle anchoring and dispersion.[2,15,16] However, such acid-site-support-induced side reactions remain a persistent challenge in (de)hydrogenation reactions, motivating ongoing development of alternative catalyst support materials.[2,17]

Liquid organic hydrogen carrier (LOHC) systems offer a versatile technical option for the safe and energy-dense transportation of hydrogen.[18] The concept builds on the binding of hydrogen through an exothermic catalytic hydrogenation reaction to the hydrogen-lean form of liquid carrier molecules, producing its hydrogen-charged counterpart. From this hydrogen-rich storage molecule, hydrogen can be released in an endothermic catalytic dehydrogenation reaction, whereby the hydrogen-lean compound is regenerated and can be used for another storage cycle.

In LOHC dehydrogenation, side reactions induced by acidic support sites are particularly problematic, leading to coking, polymerization, and C−C bond cleavage of the carrier molecule.[19−21] Among the most promising LOHC systems is the perhydro benzyltoluene/benzyltoluene (H12-/H0-BT) pair, owing to its favorable hydrogen storage properties and compatibility with existing infrastructure, allowing for a quick transition from fossil fuels.[22−24] Industrially, the dehydrogenation of perhydro benzyltoluene is catalyzed by sulfur-doped platinum nanoparticles on an alumina support, where sulfur doping reduces side product formation and increases activity.[25] However, especially at higher degrees of dehydrogenation, further reactions of the aromatic carrier molecule come into account. Deep dehydrogenation of H0-BT can lead to ring closure, forming methyl fluorene (MeFl), and subsequent polymerization toward coke precursors (CP) and coke on the catalyst surface (Figure 1). The formation of MeFl is closely related to the Pt-catalyzed dehydrogenation, whereas the CP formation is mostly influenced by the support sites.[26,27] Coking is a major cause of deactivation in dehydrogenation catalysts.[28,29] Moreover, further dehydrogenation beyond H0-BT is irreversible under typical process conditions, thereby reducing the reusability of the carrier in repeated hydrogenation−dehydrogenation cycles.[26] Thus, minimizing side product formation simultaneously decreases catalyst deactivation and enhances the long-term stability of the LOHC system. In this regard, replacing the support material with an inert alternative, such as carbon, represents a promising approach.

The hydrogenation of hydrogen-lean LOHC compounds, corresponding to the storage of hydrogen, is predominantly catalyzed by a variety of noble metal catalysts.[28,30] The use of dual-function catalysts, which are capable of catalyzing both hydrogenation and dehydrogenation, can enable compact, integrated LOHC units for stationary reversible storage in which hydrogenation and dehydrogenation are carried out at the same location and within a single reactor setup.[31,32] Such catalysts can reduce equipment count and simplify operation in stationary or stand-alone applications.[33,34] However, in many transport-oriented LOHC supply chain concepts, hydrogenation and dehydrogenation are spatially decoupled, and catalysts are generally optimized for each reaction.[35] Nevertheless, integrated "one-reactor" concepts have been demonstrated for stationary LOHC energy storage, in which hydrogenation and dehydrogenation are performed at the same site using the same catalyst and reactor hardware, enabling a compact unit for reversible storage and release.[33,34] Such integrated operation can be particularly attractive where hydrogen is charged and discharged locally to buffer mismatches between renewable energy generation and energy demand, thereby reducing system complexity and equipment

https://doi.org/10.1021/acssuschemeng.6c00102
ACS Sustainable Chem. Eng. 2026, 14, 8210−8220

count compared to fully decoupled loading/unloading infrastructures.[31,32] To date, although several dual-function catalysts have been reported, most have been engineered for application in either hydrogenation or dehydrogenation processes, rather than for both.[28,30,31] Moreover, recent research efforts have focused on enhancing mass and heat transfer in LOHC processes through structured reactor designs and optimized flow configurations.[36−40]

In this work, we present the successful integration of two solutions: a low side-product-forming carbon-based catalyst for the dehydrogenation of perhydro benzyltoluene and a robust carbon coating on an additive-manufactured stainless steel catalytic static mixer (CSM), enabling its application in continuous processes. Additionally, we present a dual-function catalyst system that outperforms industrial benchmarks under the investigated hydrogenation and dehydrogenation conditions, enabling efficient hydrogen storage and release within a single reactor setup. This system offers substantial ecological and economic advantages, positioning it as a promising solution for utilization in sustainable stationery and standalone hydrogen storage applications.

2. EXPERIMENTAL SECTION

2.1. Catalyst Preparation

The static mixers were acquired from Precision Catalysts, Victoria, Australia. They are manufactured from 316L stainless steel by selective laser melting, with a diameter of 10 mm and lengths of either 125 or 250 mm. The 5 wt % platinum on Vulcan XC-75 (Pt/CB) catalyst was acquired from Fuel Cell Store (USA) (BET surface area: 229 $m^2\ g^{-1}$). The 5 wt % platinum on alumina powder (Pt/Al_2O_3) was acquired from Sigma-Aldrich (Australia) (BET surface area: 150 $m^2\ g^{-1}$). These two catalysts were used to prepare coated CSM, denoted as Pt/CB-CSM and Pt/Al_2O_3−CSM. The catalytic coating was applied via a wash coating method, as described in our previous work.[41] The sulfur-doped platinum on alumina pellets (S−Pt/γ-Al_2O_3−pellets with 0.35 wt % Pt and 0.1 wt % S), the platinum−palladium on alumina pellets (Pt−Pd/Al_2O_3−pellets with 0.2 wt % Pt and 0.6 wt % Pd, total active metal loading of 0.8 wt %), and the perhydro benzyltoluene (H12-BT) were provided from Hydrogenious LOHC Technologies (Erlangen, Germany). Benzyltoluene (H0-BT) was acquired from Global Oil Company (Europe) (Staffordshire, UK) and dechlorinated as reported previously.[42,43]

2.2. CSM Characterization

Scanning electron microscopy combined with energy dispersive X-ray spectroscopy (SEM-EDX) images of a Pt/CB-CSM offcut were recorded on a Merlin Zeiss Gemini 2 after sputtering with Iridium for 45 s prior to SEM analysis. Optical images were captured on a laser confocal optical microscope, an Olympus OLS 5000. The offcut was manufactured along with the full CSM, coated in resin, and cut to achieve vertical cross sections for imaging. The Pt on carbon TEM specimens were prepared via drop cast and were examined using a FEI Tecnai 12 transmission electron microscope at 120 kV. Images were recorded using a FEI Eagle 4k × 4k CCD camera. The platinum loadings were determined by inductively coupled plasma optical emission spectroscopy (ICP-OES) analysis (Varian 730-ES ICP-OES). Nitrogen physisorption measurements of coated CSM offcuts were collected on a Quantachrome Autosorb iQ. Samples were degassed at 250 °C for 16 h under vacuum. The surface area was determined by nitrogen adsorption using the multipoint Brunauer−Emmett−Teller (BET) method. The blank CSM offcuts were also measured, and their respective absolute surface area was deducted. CO pulse chemisorption measurements were carried out on a Micromeritics ChemiSorb 2750.

The coating stability was confirmed by a three-step testing protocol with the sample weight recorded after each step: Initially, the CSM was subjected to 10 drops from a height of 15 cm on a metal tray. Subsequently, the CSM was subjected to heat curing at 300 °C for a duration of 1 h, after which it was subjected to a second drop test. Finally, the CSM was sonicated in cyclohexane for a period of 10 min, then dried at 120 °C and reweighed to assess coating adhesion.

2.3. Hydrogenation of Benzyltoluene

Continuous hydrogenation reactions were performed in a single-tube CSM reactor from Precision Catalysts, designed to house 10 mm diameter CSMs. The reactor had a total length of 800 mm, with five heating zones covering 650 mm. It was equipped with blank 125 mm CSMs at the top and bottom and either CSMs or pellets in between. A simplified reactor diagram is shown in Figure S1 (SI). The reactor was operated in a downflow configuration up to 200 °C, with feed rates ranging from 0.50 to 3.0 mL/min at a pressure of 20 barg. Prior to experiments, the catalyst was dried at 120 °C under hydrogen overnight. Before each run, the reactor was filled with feed solution, pressurized to 20 barg, and then heated to the target temperature under the desired feed flow.

The reaction was monitored by liquid product sampling and analysis. Samples were taken periodically through a sampling valve and analyzed by refractive index measurement on a Rudolph Refractometer J457 and by GC-FID on an Agilent 7890 GC System with FID and Column: BPX70, SGE Analytical Science, 30m length, 0.32 mm internal diameter, 0.25 μm film thickness for verification and side product formation. Correlation between refractive index and degree of dehydrogenation (DoDH) was previously reported by Geißelbrecht and conducted with a custom calibration for the refractometer.[44] Space−time yields (STY) are calculated by the formula in eq 1.

Equation 1 is the space−time yield (STY) equation, where Q is the volumetric flow rate of the feed, d is the density, M is the respective molar masses, and V is the reactor volume.

$$\mathrm{STY} = Q_{\mathrm{H0-BT}} \times d_{\mathrm{H0-BT}} \frac{M_{\mathrm{H12-BT}}}{M_{\mathrm{H0-BT}}} \frac{\mathrm{DoH}}{V_{\mathrm{reactor}}} \tag{1}$$

2.4. Dehydrogenation of Perhydro benzyltoluene

Continuous dehydrogenation reactions were also performed in a single-tube CSM reactor from Precision Catalysts, designed to house 10 mm diameter CSMs. The reactor had a total length of 500 mm, with two heating zones covering 400 mm. It was equipped with blank 125 mm CSMs at the top and bottom and a coated 250 mm CSM in between. The S−Pt/Al_2O_3 pellets were packed above a 125 mm blank CSM, with glass wool on top. A simplified reactor diagram is shown in Figure S1 (SI). Detailed information on the reactor and its setup had been reported previously.[45,46] The reactor was operated in a downflow configuration at 300 °C, with feed rates between 0.10 and 0.54 mL/min and a pressure of 2 barg. Prior to experiments, the catalyst was dried at 120 °C under hydrogen overnight and then heated to 300 °C before starting the feed. Liquid samples were periodically withdrawn through a sampling valve and analyzed by refractive index and by GC-FID. Space−time yields (STY) for the dehydrogenation reactions are calculated by the formula in eq 2.

Equation 2 is the pseudo-second order equation for the deactivation model. $y(t)$ is the space−time yield at time t, y_0 is the initial space−time yield, y_∞ is the residual (asymptotic) space−time yield at long times, and k_d is the pseudo-second-order deactivation rate constant (units of t^{-1}). Larger k_d values correspond to a faster decay of $y(t)$.

$$y_{(t)} = \frac{y_0 - y_\infty}{1 + k_d \times t} + y_\infty \tag{2}$$

3. RESULTS AND DISCUSSION

3.1. Coating Stability and Morphology

The stability test for adhesion of the CB coating to the static mixer shows lower stability than that of a conventional Al_2O_3 coating in the initial drop test, with a relative coating mass loss

https://doi.org/10.1021/acssuschemeng.6c00102
ACS Sustainable Chem. Eng. 2026, 14, 8210−8220

of 3%, Figure 2. The conventional Pt/Al_2O_3−CSM reference system, including coating/support morphology and textural

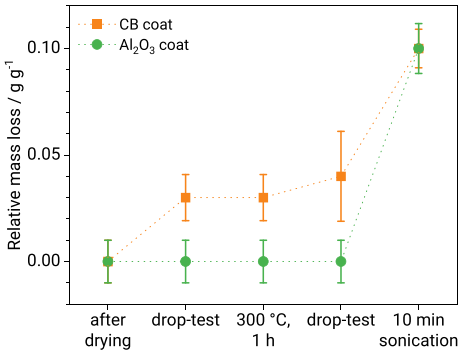

Figure 2. Stability of the coat through the stability testing algorithm for the presented CB coat and a conventional Al_2O_3 coat. For each coat, three CSM offcuts were examined. Relative mass loss is calculated by eq S1 (SI). Dotted lines provide enhanced visibility.

properties, has been characterized in detail in our previous work, and the robustness of alumina-coated CSMs has likewise been demonstrated previously under relevant operating conditions.[47,48] Following heat treatment and the subsequent second drop test, the stability further decreased by an average of 1% at each step. Sonication led to a further reduction in the coating mass, resulting in a total coating loss of approximately 10%. In contrast, the Al_2O_3 coating shows no loss during the first drop test, heat treatment, or the second drop test. Only sonication results in an overall loss of 10% of the coating. Overall, while the CB coating exhibited lower stability during the initial drop test, its overall performance was comparable to that of conventional Al_2O_3 across the full sequence of stability tests. Nevertheless, the stability test that was conducted arguably overstated the requirements for a laboratory-scale application. However, it is imperative to recognize that the stability of coat adhesion to a static mixer is a critical consideration in industrial applications, where catalysts are expected to demonstrate greater resilience than in standard laboratory settings.

As illustrated in Figure 3, the Pt/CB-CSM is shown in three stages: (A) prior to coating, (B) after coating with Pt/CB, and (C) after 44 h of operation; (D) shows a vertical cross section. The carbon coating uniformly covers the whole CSM metal surface, with only minor imperfections resulting from handling during the manufacturing process. The carbon coating fills the gaps between the metal printed structure, thereby blocking the side channels. It was ascertained that no occlusion of the vertical diamond-shaped channels occurred, thereby maintaining the primary flow characteristics. The carbon coating exhibits minor surface cracking, which increases the exposed surface area. However, the coating remains stable under the reaction conditions and throughout the stability test presented above. The cross-sectional image of the Pt/CB-CSM demonstrates the uniformity of the coating across the full diameter of the CSM, with complete coverage of internal metal scaffold surfaces.

Through the reaction, the surface structure remains unaltered, with the exception of superficial abrasions observed on the exterior of the CSM. These occur during fitting the CSM into the reactor and demonstrate a tight fit, which, in turn, promotes effective heat transfer to the metal scaffold.

The SEM images in Figure 4A show coating thicknesses ranging from 115 to 222 μm, with uniform coating-metal surfaces. As the optical images demonstrate, cracks within the coating manifest as channels, thereby allowing direct contact of the reaction media with the metal surface. The interface between the CB coating and stainless steel CSM shows no visible gaps or defects (Figure 4B). Furthermore, the SEM-EDX images (Figure 4C) reveal a uniform carbon distribution within the coating layer, indicating the absence of a density gradient or defects. This confirms that the coating is uniform and in direct contact with the metal surface.

3.2. Continuous Flow Hydrogenation of Benzyltoluene

The Pt/CB-CSM and Pt/Al_2O_3−CSM were benchmarked against commercial Pt−Pd/Al_2O_3−pellets in H0-BT hydrogenation. The reactor bed and active metal loadings are given in Table 1. Space−time yields (STY) were calculated from experiments conducted at different temperatures and are plotted in Figure 5. The reactor was initially heated to 140 °C to reach the first steady-state value in all experiments. All catalysts demonstrated elevated levels of activity, resulting in elevated reactor temperatures at steady state. Temperature rises of up to 20 °C were observed due to the exothermic nature of the reaction. For Pt/CB-CSM, insufficient heat dissipation was observed inside the reactor. STY values were therefore reported at their respective actual reactor temperature, rather than the initial heating set point. Nevertheless, temperatures remained stable at the measurement points, enabling a meaningful evaluation and comparison of catalyst performance.

As shown in Figure 5, the Pt/CB-CSM achieved the highest STY of the three catalyst systems, outperforming the Pt/Al_2O_3−CSM by 3-fold at 3 mL/min, 4-fold at 1 mL/min, and

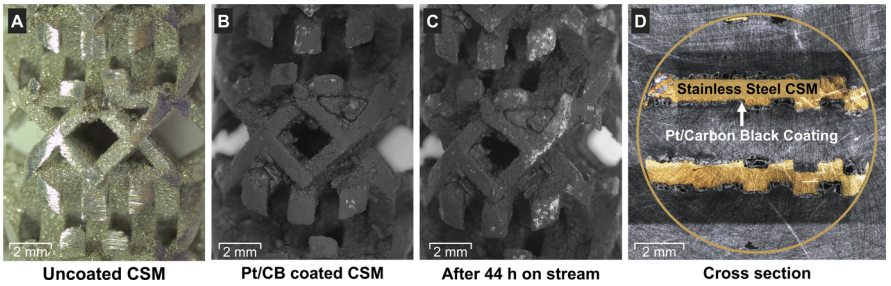

Figure 3. Microscope images of (A) uncoated static mixer, (B) Pt/CB-coated CSM before placement in the reactor, and (C) Pt/CB-coated CSM after 44 h on stream. Visible are the scratches on the CSM surface through the contact to the reactor wall ensuring heat transfer. (D) Microscope image of vertical cross section of a Pt/CB-coated CSM embedded in resin. The golden circle indicates the CSM outline. The Pt/CB coating is visible as white/black lining around the golden colored CSM. The differences in the resin's grayscale are an artifact of the picture assembly.

https://doi.org/10.1021/acssuschemeng.6c00102
ACS Sustainable Chem. Eng. 2026, 14, 8210−8220

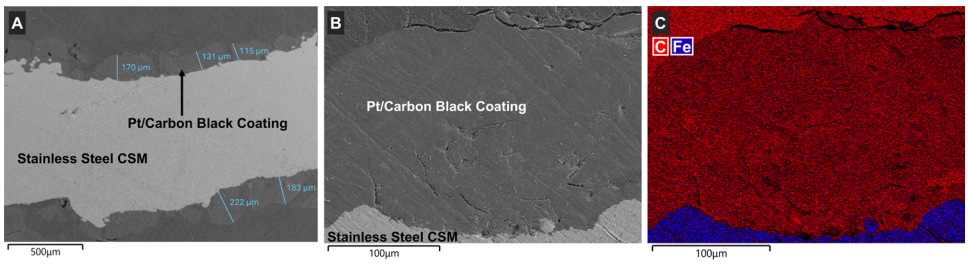

Figure 4. SEM-EDX images of the Pt/CB coating on the CSM. (A) SEM image of a metal scaffold cross section with measured coating thicknesses. (B) SEM image of the CB coating with the CSM is shown at the image bottom. (C) SEM-EDX image of the same image section as (B). The sample was embedded in resin, leading to carbon signals in the background.

Table 1. Reactor Specifications for the Hydrogenation Catalysts[a]

catalyst	$L_{\text{catalyst bed}}$ [mm]	FVF [%] free volume fraction	m_{metal} [mg]	AMD [mg/mL] active metal density	AMC [mmol/L] active metal concentration
Pt/Al_2O_3–CSM	500	75	146.4	3.7	19.1
Pt/CB-CSM	250	75	49.7	2.5	13.0
Pt–Pd/Al_2O_3–pellets	440	56	69.0	2.0	16.6

[a]AMD and AMC are calculated per reactor volume; m_{metal} is based on the total amount of catalytically active metal species Pt and Pd. Comparisons between CSM and pellet fixed-bed configurations are made at identical operating conditions based on achieving comparable degrees of hydrogenation.

nearly 3-fold at 0.5 mL/min (160 ± 3 °C). Compared to the commercial standard Pt–Pd/Al_2O_3–pellets, the Pt/CB-CSM showed 6-fold higher STY at 0.5 mL/min and 7-fold higher STY at 1 mL/min, at 160 ± 3 °C. The Pt/CB-CSM catalyst also achieved the highest degree of hydrogenation (DoH), reaching 98.6% at 167 °C and 99.3% at 172 °C at a flow rate of 0.5 mL/min. At a 1 mL/min flow, a DoH of 94.0% at 183 °C was achieved (Figure 5B). Furthermore, the Pt/CB-CSM required the shortest catalyst bed with 250 mm and the lowest active metal concentration (AMC) of 13.0 mmol/L.

The STY is dependent on the active metal content within the reactor, so higher AMC leads to higher STY. In the absence of particle size changes or interactions, this correlation is linear. Between the two CSM-based systems, the Pt/Al_2O_3–CSM has a 1.5-fold higher AMC. Given that both CSM-based catalysts are coated on the same scaffold, there are no disparities in either heat conductivity or flow mechanics assumed. Even with lower AMC, the Pt/CB-CSM outperforms the Pt/Al_2O_3–CSM by three to 4-fold. The better performance is presumably associated with improved particle distribution and stronger particle-support interactions. Consistent with this interpretation, the site-normalized hydrogenation TOF is over five times higher for Pt/CB-CSM (2.96 s^{-1}, 187 °C) than for Pt/Al_2O_3–CSM (0.58 s^{-1}, 183 °C) under their respective highest-productivity conditions (3 mL min^{-1}). Even with double the catalyst bed size, the Pt/Al_2O_3–CSM could only achieve a DoH of 78% at the lowest flow of 0.5 mL/min. The Pt–Pd/Al_2O_3–pellets have the lowest active metal density (AMD) in the sample set, but the AMC is 28% higher than the Pt/CB-CSM due to its bimetallic composition. Despite the higher AMC, the pellets resulted in the lowest STYs for all of the reaction conditions. The 76% longer catalyst bed than Pt/CB-CSM allowed a maximal DoH of 43% (178 °C with 0.5 mL/min). The markedly higher reactor productivity of the Pt/CB-CSM (six- to 7-fold outperformance in STY) is attributed primarily to improved heat management and reduced transport limitations enabled by the structured CSM architecture; the larger pressure drop of the pellet bed mainly represents an operability constraint that can limit achievable throughput rather than a direct kinetic advantage.[12] Catalytic increases up to 7-fold have been observed by Zhu et al. for the hydrogenation of vinyl acetate when comparing packed bed to CSM-catalysts.[12] The Pt/CB-CSM has the most efficient use of active metal, allowing the smallest catalyst bed and the highest DoH under the tested reaction conditions. In conclusion, the better heat conductivity and more favorable

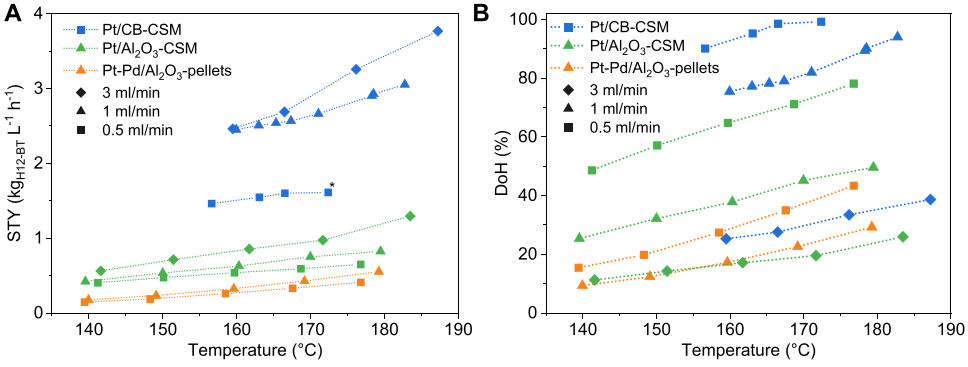

Figure 5. (A) Space–time yields (STY) of the three catalysts for H0-BT hydrogenation under 20 barg H2-pressure. Experiments were conducted in a downflow configuration. For the Pt–Pd/Al_2O_3–pellets, no experiment for 3 mL/min was conducted. *Product stream reached a DoH of 99.3%. (B) DoH values of the product stream for the respective experiment flows and temperatures.

https://doi.org/10.1021/acssuschemeng.6c00102
ACS Sustainable Chem. Eng. 2026, 14, 8210–8220

Table 2. TEM Particle Distributions and CO Pulse Adsorptions[a]

catalyst	$\mu_{TEM\text{-}virgin}$ [nm]	$\sigma^2_{TEM\text{-}virgin}$ [nm^2]	MSA [m^2 g$_{Pt}^{-1}$]	$CO_{adsorbed}$[μmol g$_{sup}^{-1}$]	CO/Pt [mol mol^{-1}]	$\mu_{TEM\text{-}44h}$ [nm]	$\sigma^2_{TEM\text{-}44h}$ [nm^2]
Pt/CB-CSM	2.44	0.65	208	81.0	0.84	2.56	1.25
Pt/Al_2O_3−CSM	3.52	1.24	83	51.1	0.34	3.85	1.78
S−Pt/Al_2O_3−pellets	1.54	0.33	294	21.4	*	*	*

[a]μ is the arithmetic mean of the TEM particles, σ^2 is the variance; MSA: active metal surface area per gram of metal; *, no post-TEM/CO was recorded for the commercial catalyst.

platinum particle distribution result in a better-performing catalytic system.

3.3. Continuous flow dehydrogenation of Perhydro benzyltoluene

The dehydrogenation of H12-BT was benchmarked against that of S−Pt/Al_2O_3−pellets. To compensate for the higher reactor volume occupied by the pellets compared to the CSM, the catalyst bed of the S−Pt/Al_2O_3−pellets was increased to 296 mm, which allowed the same residence times at the same flow rates for all catalyst systems (Table 3).

Table 3. Reactor Specifications for the Dehydrogenation Catalysts[a]

catalyst	$L_{catalyst\ bed}$ [mm]	FVF [%] free volume fraction	m_{Pt} [mg]	AMD [mg/mL] active metal density	AMC [mmol/L] active metal concentration
Pt/CB-CSM	250	75	49.7	2.5	12.8
Pt/Al_2O_3−CSM	250	75	73.5	3.7	19.0
S−Pt/Al_2O_3−pellets	296	56	35.0	1.5	7.7

[a]$L_{catalyst\ bed}$ is the length of the catalyst bed, $V_{Reactor\ empty}$ is the empty reactor space not occupied by the catalyst and its supporting structure, m_{Pt} is the amount of Platinum in the reactor, A_{BET} is the BET surface area, and $V_{Reactor}$ is the reactor volume.

Platinum Particle Size Analysis. Particle size distributions were investigated before and after use in H12-BT dehydrogenation. In addition, the XRD patterns of all virgin catalyst systems were recorded and are provided in the Supporting Information. The patterns show the broad reflections characteristic of poorly crystalline γ-Al_2O_3, while no distinct Pt- or Pt-containing reflections could be reliably resolved because of the low metal loading, small particle size, and overlap with the support. Therefore, the Pt particle size analysis was based on TEM. The particle size information was obtained using TEM images, and the results are plotted in Figure 6. For the CSM-coated catalyst systems, measurements were taken for the virgin catalysts and after 44 h of dehydrogenation. For visualization purposes, log-normal distributions were fitted to the particle size data distributions. Mean particle distributions are summarized in Table 2. ICP-OES measurements were conducted for all virgin catalysts and after 44 h on stream for the CSM-catalyst systems. No loss of platinum could be detected within the error range for the CSM-based catalysts. Absolute platinum loadings of the catalysts are listed in Figure 6B. CO pulse chemisorption analysis was executed for coated offcuts of the initial catalysts and the S−Pt/Al_2O_3−pellets. The mean TEM particle sizes correlate well with the results from the CO pulse chemisorption measurements (Table 2): the active metal surface area (MSA) per gram of Pt was derived from the adsorbed CO on the catalyst. The S−Pt/Al_2O_3−pellets had the smallest platinum particles (1.54 nm) and the highest MSA with 294 m^2 g$_{Pt}^{-1}$. The Pt/Al_2O_3−CSM exhibited a more than 2-fold larger mean particle size with 3.52 nm and, consequently, the lowest MSA with 83 m^2 g$_{Pt}^{-1}$. The Pt/CB-CSM had a mean particle size of 2.44 nm and an MSA of 208 m^2 g$_{Pt}^{-1}$. Consistently, the CO uptake (CO/Pt) was higher for Pt/CB-CSM (0.84 mol mol^{-1}) than for Pt/Al_2O_3−CSM (0.34 mol mol^{-1}), reflecting the higher fraction of accessible Pt sites associated with the smaller mean particle size and narrower size distribution.

The optimal Pt particle size for H12-BT had been reported as 2.3 nm for low temperature dehydrogenation.[29,49] The Pt/CB-CSM with a 2.44 nm mean particle size is therefore the closest to the optimal particle size. Smaller platinum particle sizes and thus higher MSA generate more active sites for the reaction, whereas an upshift in platinum particle size can be correlated to the lower activity of the Pt/Al_2O_3−CSM. Especially, as at elevated reaction temperatures the influence

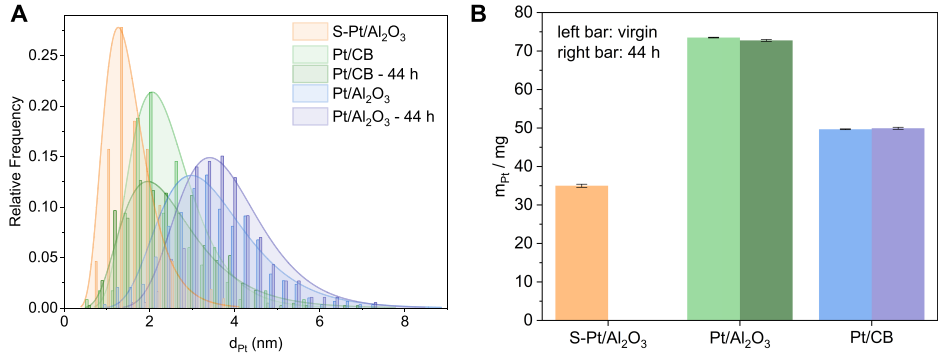

Figure 6. (A) TEM particle distributions for the catalyst before and after 44 h time on stream, fitted log-normal distributions for visualization purpose. (B) ICP measurements of the catalyst before and after catalysis are plotted as scatter. They are noted for their respective mean particle size distribution.

https://doi.org/10.1021/acssuschemeng.6c00102
ACS Sustainable Chem. Eng. 2026, 14, 8210−8220

of the MSA exceeds the geometric influence of the particle size.[29,50]

Through the 44 h on stream, the rise in mean particle size and particle distribution variance σ^2 is visible as broader and shifted log-normal curves in Figure 6A. The Pt/CB-CSM showed the highest increase in the particle size variance and an upshift of 0.12 nm of the mean particle size to 2.56 nm, Table 2. The Pt/Al_2O_3−CSM showed an increase in the mean particle size of 0.33 to 3.85 nm. The increase in mean active metal particle diameter through sintering is a common effect in platinum-based dehydrogenation catalysis, and the effects on activity are well studied.[29,30,51−53] The loss in activity throughout the 44 h on stream can be explained by the upshift of platinum particle sizes, thereby resulting in a reduction of MSA.

Dehydrogenation Activity. During the first hours of stream, STY was used to derive a deactivation model for each catalyst system. We modeled the slight initial loss in space−time yield with a power-law (pseudo-second-order) activity decay (eq 2) and the fit parameters are listed in Table 4. This assumption is also consistent with reported H12-BT dehydrogenation studies where early performance loss is strongly linked to conditioning and impurity-driven site blocking.[25,54−56] Figure 7A shows the fitted deactivation curves along with the space−time yields from the refractive index and GC-FID measurements. The high R^2 values (>0.998) demonstrate a strong correlation between the fitted and experimental data. The Pt/CB-CSM has the lowest deactivation rate (k_d), followed by Pt/Al_2O_3−CSM, and the S−Pt/Al_2O_3−pellets have nearly triple the deactivation rate, suggesting that a longer run-in period is required for the Pt/CB-CSM catalyst to reach steady state. Despite Pt/CB-CSM deactivating more slowly, Pt/CB-CSM and S−Pt/Al_2O_3−pellets have similar initial activity y_0 and residual activity y_∞.

Table 4. Fit Parameter for the Pseudo-Second Order Space−Time Yield Function[a]

catalyst	y_0[g L^{-1} h^{-1}]	k_d [h^{-1}]	y_∞[g L^{-1} h^{-1}]	R^2
Pt/CB-CSM	67 (1)	0.38 (5)	41.2 (7)	0.9992
Pt/Al_2O_3−CSM	57.8 (6)	0.50 ∞	35.3 (2)	0.9996
S−Pt/Al_2O_3−pellets	67 (4)	1.1 (3)	39.4 (6)	0.9987

[a]For deactivation calculations experiments were conducted at a residence time of 27 min.

The Pt/Al_2O_3−CSM has the lowest initial activity y_0 and residual activity y_∞ despite deactivating faster than the Pt/CB-CSM. According to the deactivation model, the Pt/CB-CSM outperformed both reference catalysts throughout the reaction time. Pt/Al_2O_3−CSM has the highest AMC (19.0 mmol/L), over 2-fold the AMC of the S−Pt/Al_2O_3−pellets (7.7 mmol/L). The high average platinum particle size of Pt/Al_2O_3−CSM (3.52 nm) leads to a lower MSA, resulting in a calculated absolute metal surface area of 6.0 m^2 for the reactor, while Pt/CB-CSM and S−Pt/Al_2O_3−pellets have a calculated absolute MSA of 10.3 m^2 for their respective reactor volume. CSM allows higher AMC and simultaneously higher FVFs. Between the two CSM-based catalysts, the 20% difference in STY results from the difference in absolute active platinum atoms, due to their difference in platinum particle size. Consistently, the site-normalized H_2 turnover frequency (2−5 h time on stream) is higher for Pt/Al_2O_3−CSM (0.96 s^{-1}) than for Pt/CB-CSM (0.67 s^{-1}), indicating higher intrinsic activity per exposed Pt site despite the lower absolute metal surface area of Pt/Al_2O_3−CSM. Regarding the STY, the Pt/Al_2O_3−CSM achieved similar results as the S−Pt/Al_2O_3−pellets, despite having a 3.5-fold lower MSA, smaller reactor volume, and no sulfurization, which increases activity.[25] The improved performance observed with the CSM-based reactor may partly arise from enhanced heat transfer and lower pressure drop, which are characteristic advantages of CSM architectures and were demonstrated in our previous work.[12,57,58] Figure 7B shows the DoDH values for the respective experiments from RI and GC measurements. The S−Pt/Al_2O_3−pellets achieved the highest DoDH, but the 36% higher reactor volume results in lower STYs than the Pt/CB-CSM. The Pt/CB-CSM has a higher AMC, although having a higher free volume fraction (FVF) than the S−Pt/Al_2O_3−pellets. With the same calculated absolute MSA for the Pt/CB-CSM and the S−Pt/Al_2O_3−pellets, the latter showed higher DoDH under the same reaction conditions, presenting the strength of the sulfurization. Additionally, the smaller platinum particle size results in better active metal use, needing 42% less platinum. On the other hand, the S−Pt/Al_2O_3−pellets exhibit the highest MSA, but increased reactor volume (due to smaller FVF), leading to a lower space−time yield than the Pt/CB-CSM. Additionally, the lower thermal conductivity of the pelletized system may negatively affect heat and mass transfer. Overall, under the investigated dehydrogenation conditions, the Pt/CB-CSM

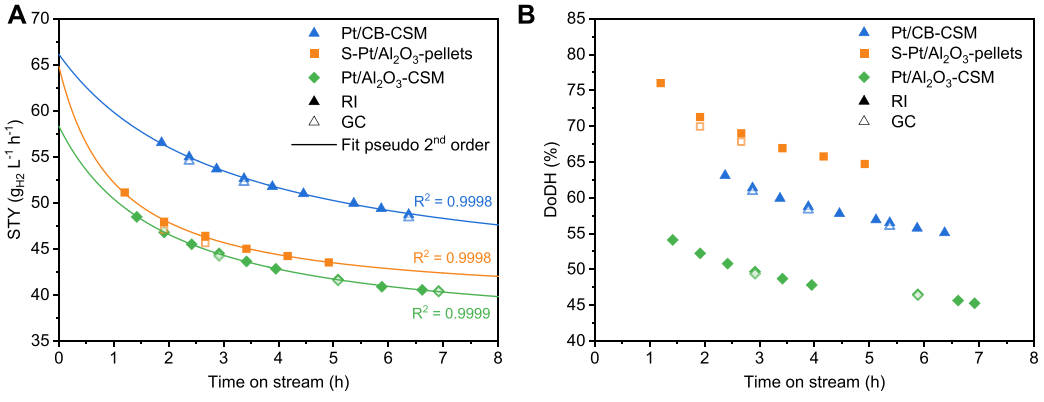

Figure 7. (A) STY for the first 7 h on stream with pseudo-second order fit for all three catalysts. For the fitting function only the refractive index measurements were considered. Residence time for all catalyst systems was 27 min. (B) DoDH for the respective experiments for all three catalysts.

https://doi.org/10.1021/acssuschemeng.6c00102
ACS Sustainable Chem. Eng. 2026, 14, 8210−8220

outperforms the S−Pt/Al_2O_3−pellets with a shorter active bed and higher space−time yield.

Side Product Formation. Methyl fluorene (MeFl) formation rates were calculated from the GC-FID measurements from different reaction conditions and are plotted in Figure 8 against the corresponding DoDH. Side product formation increases with higher DoDH, which is in accordance with the literature.[59] MeFl formation primarily occurs on low-coordinated platinum sites, and their proportion of surface atoms depends on the size of the platinum nanoparticles.[24,49,60] With increasing platinum particle size and the respective change in geometry, the amount of corner and edge-atoms reduces and thereby shifts the catalyst toward higher selectivity in H12-BT dehydrogenation. On the other hand, bigger particles reduce the MSA and overall activity. To balance between activity and selectivity, the alumina-based platinum catalysts were selectively sulfurized, resulting in the deactivation of low-coordinated platinum sites and simultaneously improving activity.[25] The S−Pt/Al_2O_3−pellets have lower MeFl formation rates at similar DoDH as the nonsulfurized Pt/Al_2O_3−CSM, showing the impact of sulfurization, despite the fact that the S−Pt/Al_2O_3−pellets have a smaller average particle diameter. The Pt/CB-CSM catalyst has a lower MeFl formation rate than the Pt/Al_2O_3−CSM catalyst despite the lower average particle diameter. The change in support material to CB shows reduced side product formation, which could be due to the absence of acidic alumina sites that catalyze side reactions.[19−21,61]

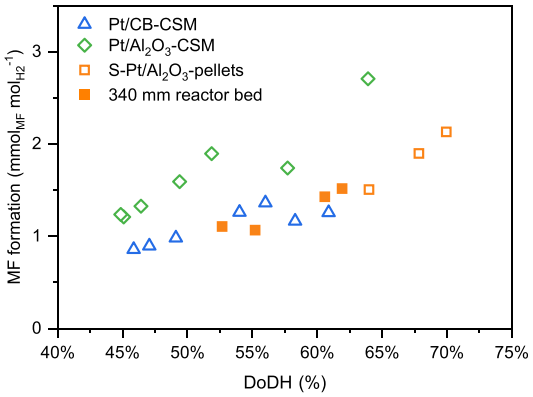

Figure 8. MeFl formation rates for the three different catalysts under investigation. Data points with filled symbols are from experiments with a catalyst bed of 340 mm.

Coke precursors (CPs) are mainly formed through reactions involving the catalyst support material.[26,27] To examine CP formation under conditions close to the reactor outlet, i.e., at high concentrations of H0-BT/at a high DoDH, a set of experiments was conducted with an artificial feed. For these experiments, we changed the feed to pure H0-BT, simulating 100% DoDH, testing all three catalyst materials under these conditions. The Pt/Al_2O_3−CSM showed the highest CP fraction, followed by the Pt/CB-CSM, while the S−Pt/Al_2O_3−pellets showed the lowest CP fraction in the GC samples. Interestingly, the S−Pt/Al_2O_3−pellets showed the most pronounced yellow discoloration of the product stream (Figure 9), indicating a higher content of side products in the samples. Generally, higher aromatic systems exhibit longer adsorption wavelengths and higher molar absorption coefficients, thereby resulting in stronger discoloration of the product stream.[62,63] It is imperative to acknowledge that the measured CP fraction reflects only the GC-detectable fraction of CP, thereby serving only as a metric for evaluating the total side product formation. Henseler et al.[26] showed that GC-FID primarily detects only dimers of the CP. Further investigation is needed to identify differences in CP formation associated with the various support materials.

The Pt/CB-CSM shows similar MeFl formation rates as the S−Pt/Al_2O_3−pellets, and it can thus be concluded that the transition to CB as a support material is an effective strategy in diminishing the formation of MeFl while maintaining a high catalytic performance. Under artificial 100% DoDH feed conditions, the Pt/CB-CSM catalyst formed fewer GC-detectable CPs than Pt/Al_2O_3CSM and avoided the strong discoloration observed for S−Pt/Al_2O_3−pellets, indicating a lower extent of undetected aromatic side products. Pt/CB-CSM combines the beneficial interaction of platinum with CB as a support with the excellent heat transfer and lower pressure drop of a CSM, resulting in a more favorable balance between activity and side product formation.

CONCLUSIONS

This study demonstrates, for the first time, the successful application of carbon-black-supported platinum catalysts as a stable and highly active catalyst coating directly on 3D printed metal mixer scaffolds. The integration of this coating with the flow- and heat-optimized CSM architecture provides a robust

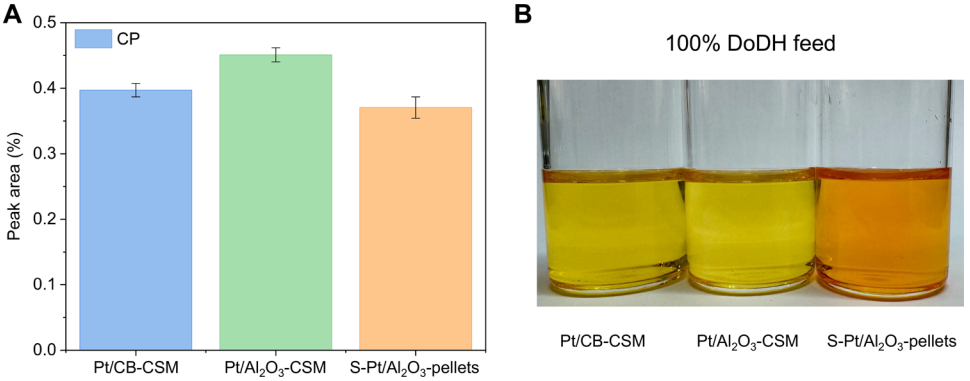

Figure 9. (A) CP peak area ratio from GC-FID measurements for the 100% DoDH feed experiments. (B) Product stream samples were obtained for 100% DoDH feed.

https://doi.org/10.1021/acssuschemeng.6c00102
ACS Sustainable Chem. Eng. 2026, 14, 8210−8220

alternative to conventional pelletized, powder bed, and slurry-based systems, enabling improved reactor performance, with the future potential to reduce pressure drop and enhance mass and heat transfer on an industrial scale. In both dehydrogenation and hydrogenation reactions, the developed system outperformed commercial benchmark catalysts, achieving up to a 7-fold increase in STY for hydrogenation and up to 16% higher STY for dehydrogenation, while simultaneously showing lower side product formation. Moreover, the dual-function capability of the catalyst system contrasts with the conventional need for separate industrial catalysts, underscoring its efficiency and versatility. These results highlight the potential of catalytic static mixer coatings for integrating noble metal catalysts into structured reactor technologies, offering improved performance for reactions using carbon-based catalysts.

■ ASSOCIATED CONTENT

Supporting Information

The Supporting Information is available free of charge at https://pubs.acs.org/doi/10.1021/acssuschemeng.6c00102.

Reactor setup and simplified flowcharts; absolute BET surface area data for carbon-black (CB) coating/catalyst loading (CSM offcuts); TEM images; powder XRD patterns (PDF)

■ AUTHOR INFORMATION

Corresponding Author

Zongli Xie − *Manufacturing, CSIRO, Clayton South, Victoria 3169, Australia;* orcid.org/0000-0002-4610-0758; Phone: +61395452938; Email: zongli.xie@csiro.au

Authors

Marcel F G Disl − *Manufacturing, CSIRO, Clayton South, Victoria 3169, Australia; Institute for a sustainable Hydrogen Economy (IHE-3), Forschungszentrum Jülich GmbH, Jülich 52428, Germany;* orcid.org/0009-0004-2325-5038

Derrick Ng − *Manufacturing, CSIRO, Clayton South, Victoria 3169, Australia;* orcid.org/0000-0003-3946-0664

Jurie Swart − *Manufacturing, CSIRO, Clayton South, Victoria 3169, Australia*

Franziska Auer − *Helmholtz-Institut Erlangen-Nürnberg for Renewable Energy (IET-2), Forschungszentrum Jülich GmbH, Erlangen 91058, Germany;* orcid.org/0009-0004-5789-8365

Stephan Kiermaier − *Institute for a sustainable Hydrogen Economy (IHE-3), Forschungszentrum Jülich GmbH, Jülich 52428, Germany;* orcid.org/0009-0007-6778-0151

Monica Distaso − *Helmholtz-Institut Erlangen-Nürnberg for Renewable Energy (IET-2), Forschungszentrum Jülich GmbH, Erlangen 91058, Germany*

Peter Wasserscheid − *Institute for a sustainable Hydrogen Economy (IHE-3), Forschungszentrum Jülich GmbH, Jülich 52428, Germany; Helmholtz-Institut Erlangen-Nürnberg for Renewable Energy (IET-2), Forschungszentrum Jülich GmbH, Erlangen 91058, Germany; Lehrstuhl für Chemische Reaktionstechnik (CRT), Friedrich-Alexander-Universität Erlangen-Nürnberg, Erlangen 91058, Germany;* orcid.org/0000-0003-0413-9539

Christian H Hornung − *Manufacturing, CSIRO, Clayton South, Victoria 3169, Australia;* orcid.org/0000-0002-3678-6565

Complete contact information is available at: https://pubs.acs.org/10.1021/acssuschemeng.6c00102

Author Contributions

M.F.G.D.: conceptualization (including cover image and TOC graphic); investigation, data curation and formal analysis (refractive index, CSM-preparation, hydrogenation, dehydrogenation, CO pulse chemisorption, SEM-EDX, Nitrogen physisorption, coating stability), formal analysis (GC-FID, TEM and deactivation modeling), funding acquisition, visualization (including cover image and TOC graphic); writing − original draft, writing − review and editing. D.N.: supervision, writing − review and editing. J.S.: investigation (dehydrogenation), data curation (dehydrogenation, refractive index), writing − review and editing. F.A.: conceptualization, writing − review and editing. S.K.: conceptualization, funding acquisition, writing − review and editing. M.D.: writing − review and editing. P.W.: project administration, resources, funding acquisition, writing − review and editing. C.H.H.: conceptualization, project administration, resources, funding acquisition, writing − review and editing. Z.X.: conceptualization, project administration, resources, funding acquisition, writing − review and editing.

Funding

The authors acknowledge the funding by the German Federal Ministry of Research, Technology, and Space and the Ministry of Economic Affairs, Industry, Climate Action, and Energy of the State of North Rhine-Westphalia through the project HC-H2. CSIRO: The authors acknowledge financial support by the Science and Industry Endowment Fund (SIEF) for experimental work conducted at CSIRO's FloWorks Facility. This work was supported by an ERA Fellowship − Green Hydrogen of the German Academic Exchange Service (DAAD).

Notes

The authors declare the following competing financial interest(s): Peter Wasserscheid is co-founder and minority shareholder of Hydrogenious LOHC Technologies GmbH, Erlangen, a company that has commercialized equipment for hydrogen storage using LOHC technology.

■ ACKNOWLEDGMENTS

The authors thank Xingdong Wang (preparation of Pt/Al2O3-CSM), Julia Krstina (several dehydrogenation reactor experiments), Nicola Spencer (GC measurements), Heidi Cheng (TEM measurements), Cornelia Nesseler (running hydrogenation experiments for two catalysts), Winston Liew and Chris Sheedy (ICP-OES measurements), and Aaron Seeber (XRD measurements and crystalline phases correlation).

■ CATALYSTS/ABBREVIATIONS

S−Pt/Al2O3−pellets,Pt on Al2O3−pellets with sulfur doping; Pt−Pd/Al2O3−pellets,Pt−Pd on Al2O3−pellets; Pt/Al2O3-CSM,Pt on Al2O3 on CSM; Pt/CB-CSM,Pt on carbon black on CSM; AMC,active metal concentration; CP,coke precursor; CSM,catalytic static mixer; DoDH,degree of dehydrogenation; DoH,degree of hydrogenation; H0-BT,benzyltoluene; H12-BT,perhydro benzyltoluene; LOHC,liquid organic hydrogen carrier; MeFl,methyl fluorene; MSA,metal surface area

https://doi.org/10.1021/acssuschemeng.6c00102
ACS Sustainable Chem. Eng. 2026, 14, 8210−8220

REFERENCES

(1) Mollar-Cuni, A.; Martín, S.; Guisado-Barrios, G.; Mata, J. A. Dual role of graphene as support of ligand-stabilized palladium nanoparticles and carbocatalyst for (de)hydrogenation of N-heterocycles. *Carbon* **2023**, *206*, 314−24.

(2) Zhang, Q.; Cheng, K.; Kang, J.; Deng, W.; Wang, Y. Fischer−Tropsch Catalysts for the Production of Hydrocarbon Fuels with High Selectivity. *ChemSusChem* **2014**, *7* (5), 1251−64.

(3) Centi, G.; Perathoner, S. Catalysis, a driver for sustainability and societal challenges. *Catal. Today* **2008**, *138* (1−2), 69−76.

(4) Zhao, S.; Wang, D.-W.; Amal, R.; Dai, L. Carbon-Based Metal-Free Catalysts for Key Reactions Involved in Energy Conversion and Storage. *Adv. Mater.* **2019**, *31* (9), No. e1801526.

(5) Hassan, E. B. E.; Hoffmann, J. Review on pressure drop through a randomly packed bed of crushed rocks. *Discov Appl. Sci.* **2024**, *6* (3), 126.

(6) Hussin, F.; Hazani, N. N.; Aroua, M. K. Effect of binder ratio on the physical properties of porous carbon pellet for CO2 capture. *Materials Today: Proceedings***2023**, DOI: .

(7) Iwanow, M.; Gärtner, T.; Sieber, V.; König, B. Activated carbon as catalyst support: precursors, preparation, modification and characterization. *Beilstein J. Org. Chem.* **2020**, *16*, 1188−202.

(8) Llamas-Unzueta, R.; Montes-Morán, M. A.; Ramírez-Montoya, L. A.; Concheso, A.; Menéndez, J. A. Whey as a sustainable binder for the production of extruded activated carbon. *Journal of Environmental Chemical Engineering* **2022**, *10* (3), No. 107590.

(9) Kundra, M.; Zhu, Y.; Nguyen, X.; Fraser, D.; Hornung, C. H.; Tsanaktsidis, J. 3D printed nickel catalytic static mixers made by corrosive chemical treatment for use in continuous flow hydrogenation. *React. Chem. Eng.* **2022**, *7* (2), 284−96.

(10) Avril, A.; Hornung, C. H.; Urban, A.; et al. Continuous flow hydrogenations using novel catalytic static mixers inside a tubular reactor. *React. Chem. Eng.* **2017**, *2* (2), 180−8.

(11) Valero-Romero, M. J.; Rodríguez-Cano, MÁ; Palomo, J.; Rodríguez-Mirasol, J.; Cordero, T. Carbon-Based Materials as Catalyst Supports for Fischer−Tropsch Synthesis: A Review. *Front. Mater.* **2021**, *7*, No. 617432.

(12) Zhu, Y.; Bin Mohamad Sultan, B.; Nguyen, X.; Hornung, C. Performance study and comparison between catalytic static mixer and packed bed in heterogeneous hydrogenation of vinyl acetate. *J. Flow Chem.* **2021**, *11* (3), 515−23.

(13) Wang, Da; Wang, Z.; Li, G.; Li, X.; Hou, B. SiO 2 -Modified Al 2 O 3 @Al-Supported Cobalt for Fischer−Tropsch Synthesis: Improved Catalytic Performance and Intensified Heat Transfer. *Ind. Eng. Chem. Res.* **2018**, *57* (38), 12756−65.

(14) Kadar, J.; Gackstatter, F.; Ortner, F.; et al. Boosting power density of hydrogen release from LOHC systems by an inverted fixed-bed reactor design. *Int. J. Hydrogen Energy* **2024**, *59*, 1376−87.

(15) Pham, H. N.; Anderson, A. E.; Johnson, R. L.; et al. Carbon Overcoating of Supported Metal Catalysts for Improved Hydrothermal Stability. *ACS Catal.* **2015**, *5* (8), 4546−55.

(16) Liu, Y.; Hou, B.; Chen, C.; et al. Carbon coated cobalt catalysts for direct synthesis of middle n-alkanes from syngas. *Fuel* **2022**, *327*, No. 124889.

(17) Zhang, Q.; Kang, J.; Wang, Y. Development of Novel Catalysts for Fischer−Tropsch Synthesis: Tuning the Product Selectivity. *ChemCatChem.* **2010**, *2* (9), 1030−58.

(18) Preuster, P.; Papp, C.; Wasserscheid, P. Liquid Organic Hydrogen Carriers (LOHCs): Toward a Hydrogen-free Hydrogen Economy. *Acc. Chem. Res.* **2017**, *50* (1), 74−85.

(19) Prieto, I.; Díaz, E.; Ordóñez, S. Biobased Furanic Molecules as Potential LOHCs: Catalytic Dehydrogenation of Tetrahydrofuran. *ACS Sustainable Chem. Eng.* **2025**, *13* (7), 2793−804.

(20) Gianotti, E.; Taillades-Jacquin, M.; Rozière, J.; Jones, D. J. High-Purity Hydrogen Generation via Dehydrogenation of Organic Carriers: A Review on the Catalytic Process. *ACS Catal.* **2018**, *8* (5), 4660−80.

(21) Bocanegra, S. A.; Castro, A. A.; Guerrero-Ruíz, A.; Scelza, O. A.; de Miguel, S. R. Characteristics of the metallic phase of Pt/Al2O3 and Na-doped Pt/Al2O3 catalysts for light paraffins dehydrogenation. *Chemical Engineering Journal* **2006**, *118* (3), 161−6.

(22) Nathrath, P.; Baier, B.; Herz, N.; et al. Hydrogen release from liquid organic hydrogen carrier using plate catalysts in continuous and dynamic operation. *Chemical Engineering Journal* **2025**, *506*, No. 159878.

(23) Cabrera, G.; Mora, M.; Gil-Burgos, J. P.; Visbal, R.; Machuca-Martínez, F.; Mosquera-Vargas, E. Liquid Organic Hydrogen Carrier Concepts and Catalysts for Hydrogenation and Dehydrogenation Reactions. *Molecules* **2024**, *29* (20), 4938.

(24) Rüde, T.; Dürr, S.; Preuster, P.; Wolf, M.; Wasserscheid, P. Benzyltoluene/perhydro benzyltoluene − pushing the performance limits of pure hydrocarbon liquid organic hydrogen carrier (LOHC) systems. *Sustainable Energy Fuels* **2022**, *6* (6), 1541−53.

(25) Auer, F.; Blaumeiser, D.; Bauer, T.; et al. Boosting the activity of hydrogen release from liquid organic hydrogen carrier systems by sulfur-additives to Pt on alumina catalysts. *Catal. Sci. Technol.* **2019**, *9* (13), 3537−47.

(26) Henseler, J.; Schärfe, T.; Steffen, J.; Görling, A.; Geißelbrecht, M.; Wasserscheid, P. Detailed analysis of coke precursor formation in catalytic perhydro benzyltoluene dehydrogenation processes. *Fuel* **2025**, *398*, No. 135500.

(27) Lenoir, C.; Rohr, F.; Stöcker, M.; Ruiz, P. Insight in the mechanism of deactivation of a Pt/mordenite (MOR) catalyst during the isomerization of n-pentane 11In memory of Professor Paul Grange. *Comptes Rendus. Chimie* **2005**, *8* (3−4), 465−74.

(28) Bourane, A.; Elanany, M.; Pham, T. V.; Katikaneni, S. P. An overview of organic liquid phase hydrogen carriers. *Int. J. Hydrogen Energy* **2016**, *41* (48), 23075−91.

(29) Mahayni, Y.; Maurer, L.; Auer, F.; Hutzler, A.; Wasserscheid, P.; Wolf, M. Structure sensitivity of the low-temperature dehydrogenation of perhydro dibenzyltoluene on supported platinum nanoparticles. *Catal. Sci. Technol.* **2024**, *14* (18), 5464−73.

(30) Rao, P.; Yoon, M. Potential Liquid-Organic Hydrogen Carrier (LOHC) Systems: A Review on Recent Progress. *Energies* **2020**, *13* (22), 6040.

(31) Dai, M.; Qin, Y.; Chen, L.; Chen, X. A review of reversible hydrogenation and dehydrogenation catalysts for liquid organic hydrogen carriers. *Catal. Sci. Technol.* **2025**, *15* (8), 2440−9.

(32) Lee, J.; Park, B. G.; Sung, K.; et al. Reversible Pd Catalysts Supported on Hierarchical Titanate Nanosheets for an N -Methylindole-Based Liquid Organic Hydrogen Carrier. *ACS Catal.* **2023**, *13* (20), 13691−703.

(33) Jorschick, H.; Preuster, P.; Dürr, S.; et al. Hydrogen storage using a hot pressure swing reactor. *Energy Environ. Sci.* **2017**, *10* (7), 1652−9.

(34) Shi, L.; Qi, S.; Qu, J.; Che, T.; Yi, C.; Yang, B. Integration of hydrogenation and dehydrogenation based on dibenzyltoluene as liquid organic hydrogen energy carrier. *Int. J. Hydrogen Energy* **2019**, *44* (11), 5345−54.

(35) Lin, A.; Bagnato, G. Revolutionising energy storage: The Latest Breakthrough in liquid organic hydrogen carriers. *Int. J. Hydrogen Energy* **2024**, *63*, 315−29.

(36) Ali, A.; Rohini, A. K.; Lee, H. J. Dehydrogenation of perhydrodibenzyltoluene for hydrogen production in a microchannel reactor. *Int. J. Hydrogen Energy* **2022**, *47* (48), 20905−14.

(37) Makaryan, I. A.; Sedov, I. V. Catalytic Reactors for Dehydrogenation of Liquid Organic Hydrogen Carriers. *Russ J. Appl. Chem.* **2021**, *94* (8), 1011−21.

(38) Peters, W.; Eypasch, M.; Frank, T.; et al. Efficient hydrogen release from perhydro-N-ethylcarbazole using catalyst-coated metallic structures produced by selective electron beam melting. *Energy Environ. Sci.* **2015**, *8* (2), 641−9.

(39) Lu, A.-H.; Li, W.-C.; Schmidt, W.; Schüth, F. Fabrication of hierarchically structured carbon monoliths via self-binding and salt templating. *Microporous Mesoporous Mater.* **2006**, *95* (1−3), 187−92.

(40) Peter, B.; Stoeckel, D.; Scherer, T.; Kuebel, C.; Roth, C.; Melke, J. Impact of catalyst support morphology on 3D electrode structure

https://doi.org/10.1021/acssuschemeng.6c00102
ACS Sustainable Chem. Eng. 2026, 14, 8210−8220

and polymer electrolyte membrane fuel cell performance. *Electrochem. Sci. Adv.* **2023**, *3* (2), No. e2100121.
(41) Kundra, M.; Grall, T.; Ng, D.; Xie, Z.; Hornung, C. H. Continuous Flow Hydrogenation of Flavorings and Fragrances Using 3D-Printed Catalytic Static Mixers. *Ind. Eng. Chem. Res.* **2021**, *60* (5), 1989−2002.
(42) Mitländer, K.; Henseler, J.; Rullo, F.; et al. Continuous (hydro-)dechlorination of aromatic chloride compounds in benzyltoluene. *Int. J. Hydrogen Energy* **2025**, *128*, 674−83.
(43) Henseler, J.; Rullo, F.; Mitländer, K.; et al. Chloroorganic impurities in technical-grade benzyltoluene − Influence on its use as LOHC compound and removal strategies. *Int. J. Hydrogen Energy* **2024**, *53*, 105−13.
(44) Geißelbrecht, M. Highly efficient, low-temperature hydrogen release from perhydro-benzyltoluene using reactive distillation. *Energy Environ. Sci.* **2020**, *13*, 3119−3128.
(45) Hornung, C. H.; Nguyen, X.; Carafa, A.; et al. Use of Catalytic Static Mixers for Continuous Flow Gas−Liquid and Transfer Hydrogenations in Organic Synthesis. *Org. Process Res. Dev.* **2017**, *21* (9), 1311−9.
(46) Nguyen, X.; Carafa, A.; Hornung, C. H. Hydrogenation of vinyl acetate using a continuous flow tubular reactor with catalytic static mixers. *Chemical Engineering and Processing - Process Intensification* **2018**, *124*, 215−21.
(47) Legg, R.; Zhang, C.; Bourchier, M.; et al. Durability Study of 3D-Printed Catalytic Static Mixers for Hydrogenations in Chemical Manufacturing. *Chemie Ingenieur Technik* **2022**, *94* (7), 1017−23.
(48) Lebl, R.; Zhu, Y.; Ng, D.; Hornung, C. H.; Cantillo, D.; Kappe, C. O. Scalable continuous flow hydrogenations using Pd/Al2O3-coated rectangular cross-section 3D-printed static mixers. *Catal. Today* **2022**, *383*, 55−63.
(49) Auer, F.; Hupfer, A.; Bösmann, A.; Szesni, N.; Wasserscheidpeter, P. Influence of the nanoparticle size on hydrogen release and side product formation in liquid organic hydrogen carrier systems with supported platinum catalysts. *Catal. Sci. Technol.* **2020**, *10* (19), 6669−78.
(50) Zagoraiou, E.; Paloukis, F.; Daletou, M. K. The role of surface chemistry of modified MWCNT on the development and characteristics of Pt supported catalysts. *Nano-Structures & Nano-Objects* **2020**, *24*, No. 100566.
(51) Wu, Y.; Li, Y.; Yu, X.; et al. Insights into size effects of Pt/Al 2 O 3 catalysts on hydrogen production from methylcyclohexane dehydrogenation. *Catal. Sci. Technol.* **2024**, *14* (7), 1791−801.
(52) van Assche, A.; Especel, C.; Le Valant, A.; Epron, F. Effect of potassium and platinum contents on catalytic performance of Pt/Al2O3 monometallic catalysts for propane dehydrogenation. *Mol. Catal.* **2022**, *517*, No. 112059.
(53) Yin, P.; Hu, S.; Qian, K.; et al. Quantification of critical particle distance for mitigating catalyst sintering. *Nat. Commun.* **2021**, *12* (1), 4865.
(54) Shakor, Z. M.; Al-Shafei, E. N. The mathematical catalyst deactivation models: a mini review. *RSC Adv.* **2023**, *13* (32), 22579−92.
(55) Rullo, F.; Beier, C.-K.; Henseler, J.; et al. Pushing activity and stability of LOHC dehydrogenation catalysts by strict LOHC quality protocols. *Int. J. Hydrogen Energy* **2025**, *98*, 606−13.
(56) Champon, I.; Bengaouer, A.; Chaise, A.; Thomas, S.; Roger, A.-C. Modelling the Sintering of Nickel Particles Supported on γ-Alumina under Hydrothermal Conditions. *Catalysts* **2020**, *10* (12), 1477.
(57) Hornung, C. H.; Singh, S.; Saubern, S. Additive Layer Manufacturing of Catalytic Static Mixers for Continuous Flow Reactors. *Johnson Matthey Technology Review* **2018**, *62* (3), 350−60.
(58) Kiermaier, S.; Nathrath, P.; Easton, C. D.; et al. Methanol steam reforming using In 2 O 3 /ZrO 2 coated catalytic static mixers (CSMs). *React. Chem. Eng.* **2026**, *11*, 625.
(59) Strauch, D.; Weiner, P.; Sarma, B. B.; et al. Bimetallic platinum rhenium catalyst for efficient low temperature dehydrogenation of perhydro benzyltoluene. *Catal. Sci. Technol.* **2024**, *14* (7), 1775−90.
(60) Alconada, K.; Mariño, F.; Agirre, I.; Barrio, V. L. Exploring Perhydro-Benzyltoluene Dehydrogenation Using Sulfur-Doped PtMo/Al2O3 Catalysts. *Catalysts* **2025**, *15* (5), 485.
(61) Fernández-Morales, J. M.; Castillejos, E.; Asedegbega-Nieto, E.; Dongil, A. B.; Rodríguez-Ramos, I.; Guerrero-Ruiz, A. Comparative Study of Different Acidic Surface Structures in Solid Catalysts Applied for the Isobutene Dimerization Reaction. *Nanomaterials (Basel)* **2020**, *10* (6), 1235.
(62) Kaeswurm, J. A. H.; Scharinger, A.; Teipel, J.; Buchweitz, M. Absorption Coefficients of Phenolic Structures in Different Solvents Routinely Used for Experiments. *Molecules* **2021**, *26* (15), 4656.
(63) Lee, Y.; Jo, A.; Park, S. B. Rational Improvement of Molar Absorptivity Guided by Oscillator Strength: A Case Study with Furoindolizine-Based Core Skeleton. *Angew. Chem., Int. Ed. Engl.* **2015**, *54* (52), 15689−93.

https://doi.org/10.1021/acssuschemeng.6c00102
ACS Sustainable Chem. Eng. 2026, 14, 8210−8220